Interface Catalysts of Ni_3Fe_1 Layered Double Hydroxide and Titanium Carbide for High-Performance Water Oxidation in Alkaline and Natural Conditions

Fuzhan Song[1#], Shaun Debow[2#], Tong Zhang[1#], Yuqin Qian[1], Zhi-Chao Huang-Fu[1], Kaylee Munns[1], Sydney Schmidt[1], Haley Fisher[1], Jesse B. Brown[1], Yanqing Su[2], Zachary Zander[3], Brendan G. DeLacy[4], Mark S. Mirotznik[5], Robert L. Opila[6], and Yi Rao[1*]

[1]Department of Chemistry and Biochemistry, Utah State University, Logan, Utah 84322, USA
[2]Department of Mechanical and Aerospace Engineering, Utah State University, Logan, Utah 84322, USA
[3]U.S. Army Combat Capabilities Development Command Chemical Biological Center, Research & Technology Directorate, Aberdeen Proving Ground, MD 21010, USA
[4]Ballydel Technologies, Inc., Wilmington, DE 19803, USA
[5]Department of Electrical and Computer Engineering, University of Delaware, Newark, DE, 19711, USA
[6]Department of Materials Science and Engineering, University of Delaware, Newark, DE, 19711, USA

Abstract

Electrocatalytic oxygen evolution reaction (OER) is of importance for many renewable energy technologies. Developing a cost-effective electrocatalysts with high performance remains a great challenge. Here, we successfully demonstrate our novel interface catalyst comprised of Ni_3Fe_1-based layered double hydroxides (Ni_3Fe_1-LDH) vertically immobilized on two-dimensional MXene ($Ti_3C_2T_x$) surface. The Ni_3Fe_1-LDH/$Ti_3C_2T_x$ yielded an anodic OER current of 100 mA cm^{-2} at 0.28 V versus reversible hydrogen electrode (RHE), nearly 74 times lower than that of the pristine Ni_3Fe_1 -LDH. Furthermore, the Ni_3Fe_1-LDH/$Ti_3C_2T_x$ catalyst only require an overpotential of 0.31 V versus RHE to deliver an industrial-level current density as high as 1000 mA cm^{-2}. Such an excellent OER activity was attributed to the synergistic interface effect between the Ni_3Fe_1-LDH and $Ti_3C_2T_x$. Density functional theory (DFT) results further reveal that $Ti_3C_2T_x$ support can efficiently accelerate the electron extraction from Ni_3Fe_1-LDH and tailor the electronic structure of catalytic sites, resulting in the enhanced OER performance.

Electrocatalytic oxygen evolution reactions (OER) have been considered core reactions in renewable energy conversion and storage devices, such as water electrolyzers and metal-air batteries.[1-13] However, the OER process suffers from sluggish kinetics due to the complex multi-electron transfer during the electrochemical the process ($4OH^- + 4e \rightarrow 2H_2O + O_2$).[14-15] Improving the process requires development of high-efficiency electrocatalysts, these catalysts will significantly lower the activitaion energy required to break apart O-H bonds while forming new O=O double bonds and is critically important to accelerate the OER kinetics. Until now, NiFe-based layered double hydroxides (Ni_xFe_y-LDHs) have been regarded as promising non-noble OER catalysts due to their earth abundance, high catalytic activity, and good stability.[16-19] Previous studies of Ni_xFe_y-LDHs showed that the Fe^{3+} dopant can increase the conductivity and accelerate charge transfer from Fe sites to Ni active centers, leading to the improvement in OER catalytic performance.[20] Friebel *et al*. demonstrated that Fe^{3+} in Ni_xFe_y OOH occupies octahedral sites and shortens the metal-O bond distances, optimizes the adsorption energy of OER intermediates, and results in a low overpotential for oxygen evolution.[21] However, the previously-reported OER performance is still far from achieving an industrially-relevant current density of 1000 mA/cm^2 due to intrinsically poor conductivity, low active catalytic site availability, and a strong tendency of the Ni_xFe_y-LDHs catalysts to aggregate. Therefore, developing noble-metal free Ni_xFe_y-LDH based electrocatalysts with excellent OER performance is imperative, but quite challenging.

Recently, transition-metal-based two-dimensional (2D) materials have gained considerable research attention due to their distinctive physical and chemical properties arising from their unique thickness and rich surface functionalization.[22] It is known that the active sites of most transition-metal-based 2D materials are located at the edge sites. Hence, activating these edge sites is vital to further enhance the catalytic activity of 2D electrocatalys.[23-24] Additionally, these exposed metallic centers can be used as coordinative sites that not only decrease the energy barrier of subsequent electrochemical reactions, but also enhance the capture ability of electrolyte ions, resulting in an improvement of electrochemical reaction kinetics.[25] Recently, considerable efforts have been focused on immobilization of earth-abundant 2D catalysts onto conductive substrates to significantly improve catalytic performance.[26-30] These results show that solid supports can efficiently stabilize the 2D electrocatalyst structure, resulting in increased performance through highly exposed surfaces, and improved conductivity that enables fast charge transfer. This highlights the effect of solid supports on improving catalytic activities of 2D electrocatalysts.

Pioneered by Gogotsi and co-workers,[31] MXene, a novel family of transition metal carbides/nitrides/carbonitrides, has attracted significant research interest for their potential energy-related applications, particularly in super-capacitors and batteries.[32-39] MXene has a general formula of $M_{n+1}X_nT_x$, where M represents an early transition metal, X for carbon or nitrogen, and T stands for the functional groups such as -OH, -O, -Cl, and –F. MXenes are particularly well-suited for energy and catalytic applications, due to their high electron conductivity and highly hydrophilic surfaces, with the $Ti_3C_2T_x$ analog being particularly well-regarded as a promising candidate to support metallic electrocatalysts.[40-42] Recently, Yue et al. successfully immobilized NiCoP on $Ti_3C_2T_x$ nanosheets through an in-situ interface-growth strategy combined with subsequent phosphorization, by virtue of the rich functional groups on the $Ti_3C_2T_x$ surface.[43] The resultant NiCoP was vertically grown on a planar $Ti_3C_2T_x$ surface, thus producing more catalytic sites. Such a novel structure efficiently accelerates charge transfer and enhances synergistic effects between NiCoP on $Ti_3C_2T_x$, resulting in improved catalytic performance.[43] Inspired by these unique properties of $Ti_3C_2T_x$, we designed a novel strategy to immobilize Ni_xFe_y-LDH on $Ti_3C_2T_x$ and constructed well-defined hierarchical 2D sandwich structures for electrocatalytic water oxidation. In this work, $Ti_3C_2T_x$ served as a 2D substrate not only to enhance the conductivity of the electrocatalyst, but also enabled Ni_xFe_y-LDH to be vertically-grown on the $Ti_3C_2T_x$ surface, thus supplying more catalytic sites for subsequent water oxidation. In addition, the Ti sites on $Ti_3C_2T_x$ were used as donor sites to stabilize the Ni^{3+} in Ni_xFe_y-LDH. As a result, these novel Ni_xFe_y-LDH/$Ti_3C_2T_x$ catalysts show excellent catalytic activity, fast kinetics, and good stability towards water oxidation in alkaline and neutral medium. Significantly, the Ni_xFe_y-LDH/$Ti_3C_2T_x$ catalysts delivered industrially-relevant current densities as high as 1000 mA cm^{-2} at a low overpotential of 0.31 V vs RHE for 20 h.

X-ray diffraction (XRD) and x-ray photoelectron spectroscopy (XPS) were used to characterize structures of the obtained Ni_3Fe_1-LDH/$Ti_3C_2T_x$ as compared with that for bare $Ti_3C_2T_x$. As shown in **Figure 1a**, the broadening of the peak at the (00l) plane for $Ti_3C_2T_x$ was attributed to the Al layers being selectively etched from the pristine Ti_3AlC_2 phase, and shows that the interlayer distance was enlarged after etching. Upon immobilization of Ni_3Fe_1-LDH on the $Ti_3C_2T_x$, a set of new peaks appeared at 11.37°, 23.32°, 34.25°, 37.95°, and 55.65°, these were assigned to the (003), (006), (012), (015), and (018) planes of the Ni_3Fe_1-LDH phase, respectively. The disappearance of the peak at (00l) from the $Ti_3C_2T_x$ XRD spectrum suggests the suppressed restacking of $Ti_3C_2T_x$ sheets by Ni_3Fe_1-LDH nanostructures standing on the surface. It is noted that the Ni_3Fe_1-LDH/$Ti_3C_2T_x$ XRD spectrum exhibits weaker signals and a higher signal-to-noise ratio compared to the pristine Ti_3AlC_2 phase. This, along with the disappearance of some of the apparent peaks from the pristine sample, are attributed to an increased distance between the layers and possibly the partial collapse of the Ti_3AlC_2 structure during the delamination and solvothermal processes. XPS was further used to characterize the valence state and chemical composition of the as-prepared Ni_3Fe_1-LDH/$Ti_3C_2T_x$. As shown in **Figure S1**, the high-resolution C 1s XPS spectra were divided into C-C (284.6 eV), C-O (285.9 eV), and O-C-O bonds (288.7 eV). For the Ti 2p core level in **Figure 1b**, three doublets were observed at 458.9, 460.1, and 464.8 eV, which correspond to Ti−O $2p_{3/2}$, Ti−F, and Ti−O $2p_{1/2}$, respectively. Moreover, **Figure 1c** exhibits the Ni $2p_{3/2}$ region, where the peaks at 855.9 and 861.8 eV were attributed to Ni $2p_{3/2}$

and its satellite.[44] For the high-resolution XPS spectrum of Fe $2p_{3/2}$ core-level, the binding energies of Fe^{3+}-O and Fe^{3+}-OH occur at 709.2 and 714.5 eV, suggesting that Fe is in the oxidation state in NiFe-LDH.[45] Overall, our XRD and XPS results confirm that Ni_3Fe_1-LDH/$Ti_3C_2T_x$ has been successfully formed.

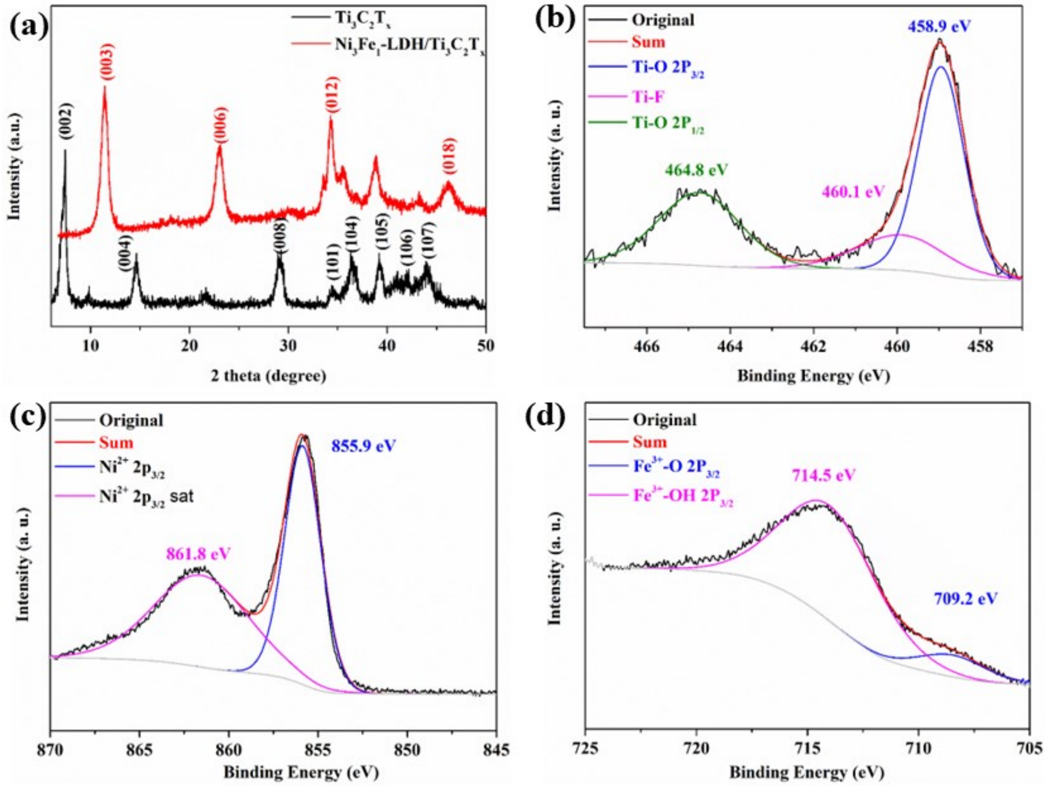

Figure 1. (a) XRD patterns for $Ti_3C_2T_x$ and Ni_3Fe_1-LDH/$Ti_3C_2T_x$. (b-d) High-resolution XPS spectra of Ti 2p, Ni $2p_{3/2}$ and Fe $2p_{3/2}$ for Ni_3Fe_1-LDH/$Ti_3C_2T_x$.

Scanning electron microscopy (SEM) and transmission electron microscopy (TEM) were used to characterize the morphology of the as-prepared Ni_3Fe_1-LDH/$Ti_3C_2T_x$. Three-dimensional interconnected Ni_3Fe_1-LDH nanoplates were found to be vertically oriented on surface of $Ti_3C_2T_x$ sheets, as shown in **Figure 2a**. TEM results in **Figure 2b** show the formation of loosely packed Ni_3Fe_1-LDH nanoplates with very thin thickness of several nm on $Ti_3C_2T_x$ surface. Furthermore, high-resolution TEM (HRTEM) in Figure 2c shows that the interlayer spacing was 0.25 nm, which corresponds to the (012) crystal plane of NiFe-LDH. The HRTEM results suggest the crystalline nature of the as-synthesized Ni_3Fe_1-LDH nanoplates, which is agreement with that of the XRD diffraction peak at 34.25°. In addition, the elemental mapping images in **Figure 2d** show spatial distributions of Ti, C, O, Ni, and Fe. Overall, these structural and morphological analyses indicate that the Ni_3Fe_1-LDH were vertically grown on $Ti_3C_2T_x$ surfaces. Such a unique 3D structure can provide favourable mass diffusion, fluent electron transport channels, and shorten ion diffusion during the OER process.

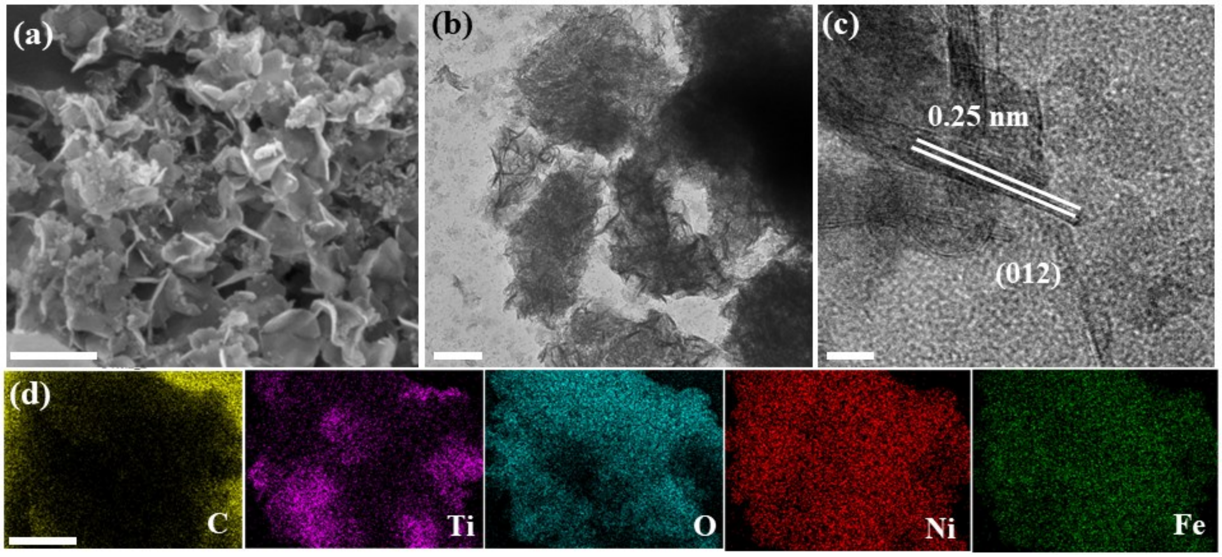

Figure 2. (a) SEM image, (b-c) TEM images and (d) elemental mapping results of Ni_3Fe_1-LDH/$Ti_3C_2T_x$. Scale bars: 200 nm (a-b); 5 nm (c); 5 µm (d).

The OER performance of Ni_xFe_y-LDH/$Ti_3C_2T_x$ was evaluated by a standard three-electrode cell in an O_2-saturated 1.0 M KOH solution. The effect of Ni/Fe molar ratio on determining oxygen performance has firstly explored. As shown in **Figure S2**, catalytic performance of the Ni_xMo_y/$Ti_3C_2T_x$ catalytic system at different ratios of Ni to Mo. Among the all Ni_xFe_y-LDH/$Ti_3C_2T_x$ system, the as-synthesized Ni_3Fe_1-LDH/$Ti_3C_2T_x$ demonstrate the highest OER current density, suggesting the Ni/Fe mole ratio can efficiently determine OER activity and the optimal Ni:Fe mole ratio is 3:1, which was close to the value of 2.89:1 from our inductively coupled plasma optical emission spectroscopy (ICP-OES) measurements, as shown in **Table S1**. The measured ratio was close to the initially added mole ratio of Ni to Fe. Furthermore, the catalytic performance of Ni_3Fe_1-LDH with various amounts on $Ti_3C_2T_x$ solid support were carried out. With the molar amount of Ni_3Fe_1-LDH increasing, the OER catalytic performance of Ni_3Fe_1-LDH/$Ti_3C_2T_x$ initially enhances, and the best catalytic performance was achieved at Ni_3Fe_1-LDH molar amount of 0.016 mmol, as shown in **Figure S3**. Further increasment will yield a decay for catalytic oxygen evolution. Therefoe, the optimal Ni_3Fe_1-LDH/$Ti_3C_2T_x$ was employed for further OER characterization unless noted otherwise. As comparisons, Ni-LDH/$Ti_3C_2T_x$, Fe-LDH/$Ti_3C_2T_x$, Ni_3Fe_1-LDH, and $Ti_3C_2T_x$ were also synthesized and examined under the same experimental conditions. The iR-corrected linear sweep voltammetry (LSV) curve was obtained by using a scan rate of 5 mV s^{-1} to minimize the capacitive current and all potentials used in this work were evaluated vs RHE. **Figure 3a** shows iR-corrected LSV curves of

Ni_3Fe_1-LDH/$Ti_3C_2T_x$, Ni-LDH/$Ti_3C_2T_x$, Fe-LDH/$Ti_3C_2T_x$, and pure Ni_3Fe_1-LDH in 1.0 M KOH solution. It is shown that the strongest oxidation peak, at 1.45 V versus RHE, was observed for Ni_3Fe_1-LDH/$Ti_3C_2T_x$ due to the oxidation reaction of $Ni^{2+} \rightarrow Ni^{3+}/Ni^{4+}$, which is considered to be the most efficient active site for catalyzing the OER in an alkaline solution. It is seen that Ni_3Fe_1-LDH/$Ti_3C_2T_x$ exhibits the best OER performance among all samples. To exclude the anodic current from redox $Ni^{2+}/Ni^{3+,4+}$, an overpotential for producing the current density of 50 mA cm^{-2} (η_{50}) was used to assess the OER activities for all the samples. As shown in **Figure 3a**, a very low overpotential of 0.26 V versus RHE was required to obtain a current density of 50 mA cm^{-2} for Ni_3Fe_1-LDH/$Ti_3C_2T_x$, while overpotentials of 0.53 and 0.65 V versus RHE for Fe-LDH/$Ti_3C_2T_x$ and Ni-LDH/$Ti_3C_2T_x$, respectively, were observed. The addition of oxided Fe ions can not only enable the electron-donating ability of the bridging intermediated oxygen species, but also stabilize the oxidized Ni lattice during the catalytic reaction.[46] More importantly, our Ni_3Fe_1-LDH/$Ti_3C_2T_x$ shows a superior OER performance over pure Ni_3Fe_1-LDH. Our Ni_3Fe_1-LDH/$Ti_3C_2T_x$ only need overpotentials of 0.26, 0.27, and 0.28 V versus RHE to deliver 50, 75, and 100 mA cm^{-2}, respectively, which are 55, 64, and 74 times higher than those for pure Ni_3Fe_1-LDH. The $Ti_3C_2T_x$ itself shows a negligible OER property across all potential windows in **Figure S4**, suggesting the enhancement is due to synergestic effects between the $Ti_3C_2T_x$ support and Ni_3Fe_1-LDH, with the support playing an important role to accelerate the OER activity for Ni_3Fe_1-LDH. Strikingly, the as-prepared Ni_3Fe_1-LDH/$Ti_3C_2T_x$ composites display an outstanding OER performance at industrially-important current density, rarely achieved in the previous reported literature.[47-53] Even for an industrial current density as high as 1000 mA cm^{-2}, our Ni_3Fe_1-LDH/$Ti_3C_2T_x$ catalyst only needs an overpotential of 0.3 V versus RHE. On the other hand, pure Ni_3Fe_1-LDH produced a low current density of 83 mA cm^{-2} at the same potential input. To further compare the intrinsic activities, turnover frequency (TOF) of Ni_3Fe_1-LDH/$Ti_3C_2T_x$, Ni-LDH/$Ti_3C_2T_x$, Fe-LDH/$Ti_3C_2T_x$, and pure Ni_3Fe_1-LDH were calculated. As expected, the as-synthesized Ni_3Fe_1-LDH/$Ti_3C_2T_x$ exhibits the highest TOF of 2.4×10^{-1} s^{-1}, which is 32, 381, and 387 times higher than those for Ni_3Fe_1-LDH (7.5×10^{-3} s^{-1}), Ni-LDH/$Ti_3C_2T_x$ (6.3×10^{-4} s^{-1}), and Fe-LDH/$Ti_3C_2T_x$ (6.2×10^{-4} s^{-1}), respectively.

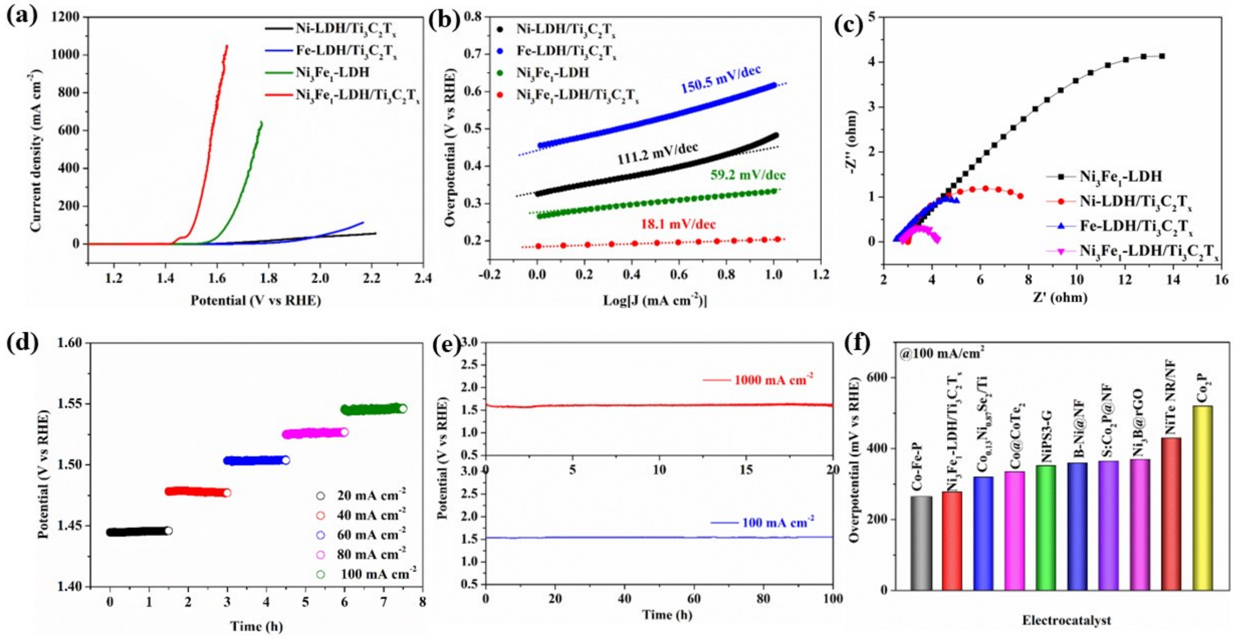

Figure 3. (a) LSV curves of Ni_3Fe_1-LDH/$Ti_3C_2T_x$, Ni-LDH/$Ti_3C_2T_x$, Fe-LDH/$Ti_3C_2T_x$, and Ni_3Fe_1-LDH in O_2-saturated 1.0 M KOH. (b) Tafel plots of Ni_3Fe_1-LDH/$Ti_3C_2T_x$, Ni-LDH/$Ti_3C_2T_x$, Fe-LDH/$Ti_3C_2T_x$, and Ni_3Fe_1-LDH in O_2-saturated 1.0 M KOH. (c) EIS spectra for Ni_3Fe_1-LDH/$Ti_3C_2T_x$, Ni-LDH/$Ti_3C_2T_x$, Fe-LDH/$Ti_3C_2T_x$, and Ni_3Fe_1-LDH at 1.558 V vs RHE. (d) Multi-step chronopotentiometry curves of Ni_3Fe_1-LDH/$Ti_3C_2T_x$ with the different current densities from 20 to 100 mA cm^{-2} for 1.5 h in O_2-saturated 1.0 M KOH. (e) Chronopotential plot of Ni_3Fe_1-LDH/$Ti_3C_2T_x$ in 1.0 M KOH. (f) Comparison of overpotentials of selected electrocatalysts to deliver 100 mA cm^{-2} for OER in 1.0 M KOH.

To reveal the reaction kinetics of OER for the electrocatalyst, Tafel slopes were obtained from their corresponding LSV curves by applying the Tafel equation ($\eta = a + b \log j$, where η, j and b represent overpotential, current density, and the Tafel slope, respectively). As shown in **Figure 3b**, the Ni_3Fe_1-LDH/$Ti_3C_2T_x$ catalyst demonstrates a Tafel slope of 18.1 mV dec^{-1}, which is much lower than those for Ni-LDH/$Ti_3C_2T_x$ (150.5 mV dec^{-1}), Fe-LDH/$Ti_3C_2T_x$ (111.2 mV dec^{-1}), and Ni_3Fe_1-LDH (59 mV dec^{-1}). Such a low value of Tafel slope suggests that the electron transfer process in the reaction ($MO + OH^- \rightarrow MOOH + e^-$, M: Ni or Fe) is the rate-determining step, where a hydroxylation reaction involving OH^- forms the OOH species.[54-55] Electrochemical impedance spectra (EIS) were also carried out to understand the OER activity of Ni_3Fe_1-LDH/$Ti_3C_2T_x$. **Figure 3c** shows the Nyquist plots for Ni_3Fe_1-LDH/$Ti_3C_2T_x$, Ni-LDH/$Ti_3C_2T_x$, Fe-LDH/$Ti_3C_2T_x$, and Ni_3Fe_1-LDH. Our Ni_3Fe_1-LDH/$Ti_3C_2T_x$ catalysts exhibit a smallest semicircular diameter among all samples, suggesting that a faster charge-transfer rate was achieved for Ni_3Fe_1-LDH/$Ti_3C_2T_x$. It is known that OER process suffers from sliggish kinetic rates due to its intrinsic four electron process in alkaline media ($4OH^- + 4e \rightarrow 2H_2O + O_2$). The low resistance of our Ni_3Fe_1-LDH/$Ti_3C_2T_x$ catalyst improves charge transfer between the electrode/electrolyte and accelerates the intrinsic kinetics for oxygen evolution. Stability of electrocatalyst is one of the most important parameters to consider when assessing the potential of electrode materials to be used in commercial applications. Multiple-current chronopotentiometry experiments were performed to examine the rapid -response rate of carrier migration, as revealed in **Figure 3d**. Attention was only paid to the relatively high current densities from 20 to 100 mA/cm^2. The observed change under applied potentials was consistent with their corresponding stable current values, confirming excellent mass transportation properties, conductivity, and mechanical robustness of the electrode.[56-57] Furthermore, controlled-current electrolysis at 100 mA cm^{-2} was also carried out to evaluate the durability of the catalysts. **Figure 3e** shows that our Ni_3Fe_1-LDH/$Ti_3C_2T_x$ can stably produce a current density of 100 mA cm^{-2} with no apparent degradation observed after 100 h. The generated O_2 amount well matched the theoretically calculated quantity, where all the passed charge was used to catalyze for O_2 generation with a Faradaic efficiency close to 100% (**Figure S5**). More importantly, our Ni_3Fe_1-LDH/$Ti_3C_2T_x$ catalysts readily drive water oxidation at high current densities of 500 and 1000 mA cm^{-2} at very low potentials of 1.57 and 1.62 V, respectively, as shown in **Figures 3e and S6**. The excellent OER performance makes our Ni_3Fe_1-LDH/$Ti_3C_2T_x$ comparable to most non-precious OER electrocatalysts reported in the literature, including Co-Fe-P,[58] $Co_{0.13}Ni_{0.87}Se_2$/Ti,[59] Co@$CoTe_2$,[60] $NiPS_3$-G,[61] B-Ni@NF,[47] S:Co_2P@NF,[62] Ni_3B@rGO,[63] NiTe NR/NF,[64] Co_2P,[65] $NiFeP_x$-NC[66], Mo/Mo_2C@CoO@NC[67], and Ti_3C_2-Co-TiO_2[68], as shown in **Figure 3f** and **Table S2**. Overall, these above results unambiguously confirm that our Ni_3Fe_1-LDH/$Ti_3C_2T_x$ demonstrates outstanding performance over the full range of current densities and possesses a robust industrially-relevant stability for water oxidation applications.

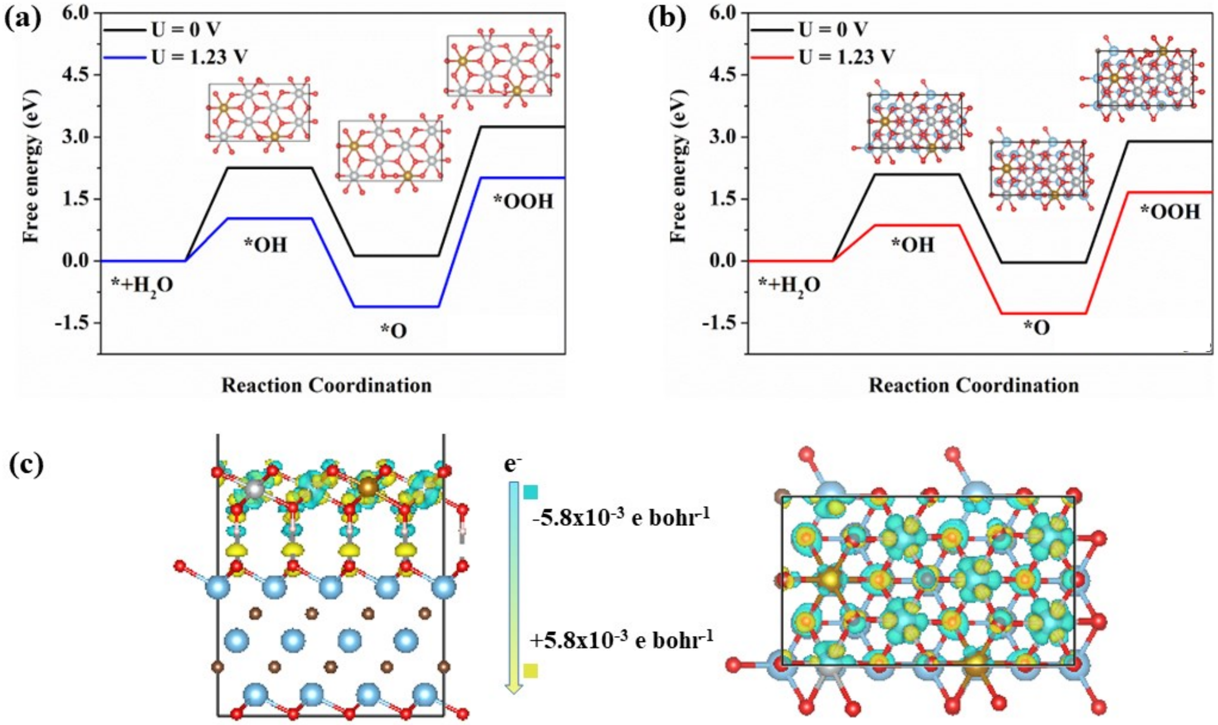

Figure 4. Free-energy diagram and corresponding intermediate species for oxygen evolution reaction over (a) Ni_3Fe_1-LDH and (b) Ni_3Fe_1-LDH/Ti_3C_2 at U = 0 and 1.23 eV. (c) Distribution of charge densities for Ni_3Fe_1-LDH/Ti_3C_2. Yellow and cyan colors denote electron accumulation ($\Delta\rho = +5.8 \times 10^{-3}$ e bohr^{-3}) and depletion ($\Delta\rho = -5.8 \times 10^{-3}$ e bohr^{-3}), respectively. Left, top view; right, side view.

To gain further insight into the mechanism of the oxygen electrocatalytic performance, density functional theory (DFT) computations were implemented to investigate the free energy diagrams of intermediated species toward the oxygen evolution process. We designed a suitable model of the Ni_3Fe_1-LDH/Ti_3C_2 interface, where the hydroxyl of Ni_3Fe_1-LDH was connected to O-terminated Ti_3C_2 through the OH-O bond and thereby stabilized the interface, in **Figure S7**. As proposed by Nørskov et al.,[69] the four-electron process of water oxidation is described as follows:

$$H_2O + * \rightarrow *OH + H^+ + e^- \qquad (I)$$

$$*OH + * \rightarrow *O + H^+ + e^- \qquad (II)$$

$$*O + H_2O \rightarrow *OOH + H^+ + e^- \qquad (III)$$

$$*OOH \rightarrow O_2 + H^+ + e^- \qquad (IV)$$

where * represents the catalytic site of an electrocatalyst. We evaluated the Gibbs free energy diagram of oxygen evolution reaction. As shown in **Figures 4a-b** and **S8-13**, for both Ni_3Fe_1-LDH/$Ti_3C_2T_x$ and Ni_3Fe_1-LDH, the second step of hydroxyl group splitting into *O species is exothermic at the applied voltage (V) = 0 and 1.23 V, while the *OH and *OOH formation exhibit uphill energetics. The energy barriers of *OOH formation were found to be 2.92 and 3.11 eV for Ni_3Fe_1-LDH/$Ti_3C_2T_x$ and Ni_3Fe_1-LDH, respectively. In general, the formation step of *OOH has been considered the rate-determining step (RDS) in the whole oxygen evolution reaction. During the rate-determining step, Ni_3Fe_1-LDH/$Ti_3C_2T_x$ exhibits only a slight energy difference of 0.19 eV from that of the Ni_3Fe_1-LDH, suggesting that generation kinetics of *OOH is not critical at the interface of Ni_3Fe_1-LDH and $Ti_3C_2T_x$. To further evaluate the synergistic effect of the interface catalysts, Bader charge analyses of the above two models were carried out. As displayed in **Figures 4c**, a large electron transfer of 5.8×10^{-3} e bohr^{-3} was observed from Ni_3Fe_1-LDH to $Ti_3C_2T_x$ solid support, which supports a more positively charged Ni_3Fe_1-LDH surface and therefore optimizes the energy barriers of the whole water oxidation process. In addition, such an electron extraction from the Ni_3Fe_1-LDH can efficiently modulate the electronic structure of catalytic sites in an Ni_3Fe_1-LDH/Ti_3C_2 hybrid, which supports the *d*-band center shifting to a high energy. Consequently, the antibonding states of catalytic sites in the hybrid system and adsorbed *O intermediated species are less occupied, thus enhancing the O binding strength for oxygen evolution process in an alkaline solution.[43, 70]

The excellent OER activity and stability of Ni_3Fe_1-LDH/$Ti_3C_2T_x$ under strong alkaline conditions prompted us to further investigate its OER performance in weak alkaline and neutral electrolytes. In particular, OER in neutral media is more practical for industrial applications. Therefore, the OER activities of Ni_3Fe_1-LDH/$Ti_3C_2T_x$ in 0.1 M KOH (pH = 13) and 1.0 M KPi (pH = 7) were evaluated. As expected, similar electrocatalytic activity trends were observed. The Ni_3Fe_1-LDH/$Ti_3C_2T_x$ catalyst exhibited a superior OER performance as compared with those for pure Ni_3Fe_1-LDH in both of 0.1 M KOH and 1.0 M KPi solution (**Figure 5**). Achieving a current density of 10 mA cm^{-2}, Ni_3Fe_1-LDH/$Ti_3C_2T_x$ only requires 1.54 and 1.79 V versus RHE in 0.1 M KOH and 1.0 M KPi, which are much lower than those for pure Ni_3Fe_1-LDH, highlighting the synergistic effect on improving oxygen catalytic performance in wide-pH electrolyte (pH = 14-7) (**Figures S14-15**). Such an enhanced performance was likely due to the fact that $Ti_3C_2T_x$ efficiently facilitates the charge transfer between Ni_3Fe_1-LDH/$Ti_3C_2T_x$.

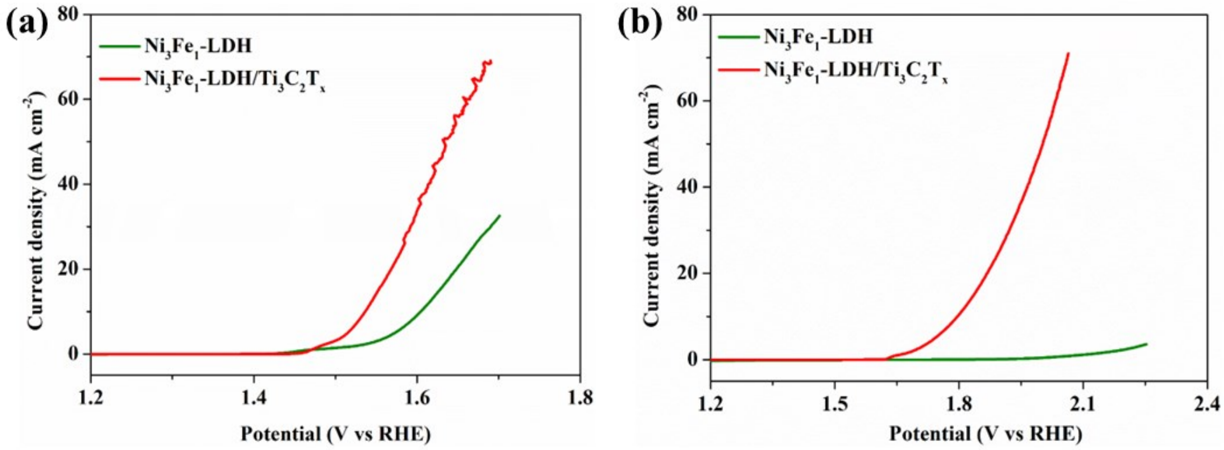

Figure 5. LSV curves of Ni_3Fe_1-LDH/$Ti_3C_2T_x$ and Ni_3Fe_1-LDH in O_2-saturated 0.1 M KOH (a) and 1.0 M KPi (b).

Overall, the above results unambiguously confirmed that our Ni_3Fe_1-LDH/$Ti_3C_2T_x$ electrocatalysts exhibit an excellent electrocatalytic performance for oxygen evolution under alkaline and neutral conditions. Such a substantial increase in catalytic activity is due to the following features: (1) Ni_3Fe_1-LDH vertically aligned on $Ti_3C_2T_x$ surface. With the rich functional groups of $Ti_3C_2T_x$ (e.g. -OH, =O, -Cl, and -F), Ni_3Fe_1-LDH was vertically immobilized on $Ti_3C_2T_x$ surface. These surface functional groups can be used as "anchor" to coordinate with metal ions, resulting in rich and uniform nucleation center for a controlled vertical growth of Ni_3Fe_1-LDH on $Ti_3C_2T_x$. Such an unique configuration can expose more layered edges of Ni_3Fe_1-LDH, which provides kinetical active sites with high valence and fluent electron transport channels for oxygen evolution.[45] More importantly, metallic $Ti_3C_2T_x$ is electrically conductive and shortens ion diffusion length, which can efficiently facilitate the charge transfer between electrode/electrolyte and accelerate the intrinsic kinetics for oxygen evolution. (2) High oxidation of Ti sites. It is reported that highly oxidated Ti^{3+} ions on the $Ti_3C_2T_x$ surface can be formed at a redox potential of 280 mV.[71] The Ti^{3+} ions can act as *n*-type dopants to optimize the electronic configuration of the Ni ions, therefore stabilizing the Ni ion with an oxidation state of 3+, which serve as highly active catalytic sites for oxygen evolution.[72] (3) Synergistic effects between Ni_3Fe_1-LDH and $Ti_3C_2T_x$. The $Ti_3C_2T_x$ solid support can extract electrons from the nearby Ni_3Fe_1-LDH, re-configurate the charge distribution of catalytic sites, and achieving the highly-efficient spatial charge separation, resulting in an electron-hole-rich area at the interfacial area. The electron-hole-rich catalytic sites can lower the energy barrier and optimize the adsorbed intermediated species for water oxidation. In addition, the electron transfer in Ni_3Fe_1-LDH/$Ti_3C_2T_x$ interface can not only optimize *d*-band center shift for enhancing the O binding strength, but also decrease the work function of catalytic sites to achieve more acceptor levels.

In this work, we have synthesized a cost-effective and robust Ni_3Fe_1-LDH/$Ti_3C_2T_x$ electrocatalyst for boosting oxygen evolution in alkaline and neutral media. By making full use of the rich surface functional groups of $Ti_3C_2T_x$, thin 2D Ni_3Fe_1-LDH layers were vertically immobilized on the $Ti_3C_2T_x$ surface. The Ni_3Fe_1-LDH/$Ti_3C_2T_x$ hybrids exhibit excellent catalytic performance for oxygen evolution in 1.0 M KOH with an overpotential of 282 mV to produce an OER current density of 100 mA cm^{-2} and a Tafel slope as low as 18.1 mV dec^{-1}. Strikingly, Ni_3Fe_1-LDH/$Ti_3C_2T_x$ only needs an overpotential of 0.31 V versus RHE to produce an industrially-important current density of 1000 mA cm^{-2}. DFT results further demonstrated $Ti_3C_2T_x$ could accelerate the charge transfer and tailor the electronic structure of the Ni_3Fe_1-LDH catalytic sites. The synergistic effect between Ni_3Fe_1-LDH and $Ti_3C_2T_x$ can optimize the *d*-band center shift, resulting in enhanced catalytic property of oxygen evolution. This work provides a facile strategy for the construction of $Ti_3C_2T_x$-based 2D layered electrocatalyst for many other applications, beyond water oxidation.

Supporting Information

The supporting information contains additional experimental details, including: chemicals; Charaterization; methods to prepare samples for characterization; instrumentation used to characterize samples; additional synthetic procedures to fabricate electrocatalysts; and, a section on density functional theory calculations and methods. The following supporting figures are provided in the supporting information: XPS spectrum of C for Ni_3Fe_1-LDH/$Ti_3C_2T_x$, **Figure S1**; LSV curves of Ni_xFe_y-LDH/$Ti_3C_2T_x$ with different Ni/Fe mole ratios in 1.0 M KOH, **Figure S2**; LSV curves of Ni_3Fe_1-LDH/$Ti_3C_2T_x$ with different Ni_3Fe_1-LDH in 1.0 M KOH, **Figure S3**; LSV curves of Ni_3Fe_1-LDH/$Ti_3C_2T_x$ and $Ti_3C_2T_x$ in 1.0 M KOH, **Figure S4**; Gas yield of O_2 evolved over the Ni_3Fe_1-LDH/$Ti_3C_2T_x$ electrodes as a function of time at 100 mA cm^{-2}, **Figure S5;** chronopotential curve of Ni_3Fe_1-LDH/$Ti_3C_2T_x$ conducted at 500 mA cm^{-2} in 1.0 M KOH, **Figure S6**; optimized structure of Ni_3Fe_1-LDH/Ti_3C_2**, Figure S7;** OH adsorption structure of Ni_3Fe_1-LDH/Ti_3C_2**, Figure S8;** O adsorption structure of Ni_3Fe_1-LDH/Ti_3C_2**, Figure S9;** OOH adsorption structure of Ni_3Fe_1-LDH/Ti_3C_2**, Figure S10;** OH adsorption structure of Ni_3Fe_1-LDH**, Figure S11;** O adsorption structure of Ni_3Fe_1-LDH**, Figure S12;** OOH adsorption structure of Ni_3Fe_1-LDH**, Figure S13;** EIS spectra for Ni_3Fe_1-LDH/$Ti_3C_2T_x$ and Ni_3Fe_1-LDH in 0.1 M KOH solution, **Figure S14**; EIS spectra for Ni_3Fe_1-LDH/$Ti_3C_2T_x$ and Ni_3Fe_1-LDH in 1.0 M KPi solution, **Figure S15**;

AUTHOR INFORMATION

Corresponding Author: Y.R. email: yi.rao@usu.edu

Author Contributions

\# F.Z.S., S.D, and T.Z., contributed equally to this work.

Notes

There are no conflicts to declare.

Acknowledgements

Y.R. acknowledges the financial support of Reactive Chemical Systems Programs, U.S. Army Research Office (W911NF18020112). Funding was provided by the U.S. Army *via* the Surface Science Initiative Program (PE 0601102A Project VR9) at the US Army, Combat Capabilities Development Command, Chemical Biological Center. This work is also supported by the National Science Foundation under Grant No.[2045084]. We also acknowledge the Microscopy Core Facility at USU for SEM measurement. The support and resources from the Center for High Performance Computing at the University of Utah are gratefully acknowledged.

Conflicts of interest

The authors declare no competing financial interest.

References

1. Yu, F.; Zhou, H.; Huang, Y.; Sun, J.; Qin, F.; Bao, J.; Goddard, W. A.; Chen, S.; Ren, Z. High-performance bifunctional porous non-noble metal phosphide catalyst for overall water splitting. *Nat. Commun.* **2018,** *9* (1), 2551, DOI: 10.1038/s41467-018-04746-z
2. Yang, F.; Han, P.; Yao, N.; Cheng, G.; Chen, S.; Luo, W. Inter-regulated d-band centers of the Ni3B/Ni heterostructure for boosting hydrogen electrooxidation in alkaline media. *Chem. Sci.* **2020,** *11* (44), 12118-12123, DOI: 10.1039/D0SC03917A
3. Song, F.; Li, W.; Yang, J.; Han, G.; Yan, T.; Liu, X.; Rao, Y.; Liao, P.; Cao, Z.; Sun, Y. Interfacial Sites between Cobalt Nitride and Cobalt Act as Bifunctional Catalysts for Hydrogen Electrochemistry. *ACS Energy Lett.* **2019,** *4* (7), 1594-1601, DOI: 10.1021/acsenergylett.9b00738
4. Ding, H.; Liu, H.; Chu, W.; Wu, C.; Xie, Y. Structural Transformation of Heterogeneous Materials for Electrocatalytic Oxygen Evolution Reaction. *Chem Rev.* **2021,** *121* (21), 13174-13212, DOI: 10.1021/acs.chemrev.1c00234
5. Zhang, T.; Debow, S.; Song, F.; Qian, Y.; Creasy, W. R.; DeLacy, B. G.; Rao, Y. Interface Catalysis of Nickel Molybdenum (NiMo) Alloys on Two-Dimensional (2D) MXene for Enhanced Hydrogen Electrochemistry. *J. Phys. Chem. Lett.* **2021,** *12* (46), 11361-11370, DOI: 10.1021/acs.jpclett.1c02676

6. Huang, Z.-F.; Xi, S.; Song, J.; Dou, S.; Li, X.; Du, Y.; Diao, C.; Xu, Z. J.; Wang, X. Tuning of lattice oxygen reactivity and scaling relation to construct better oxygen evolution electrocatalyst. *Nat. Commun.* **2021,** *12* (1), 3992, DOI: 10.1038/s41467-021-24182-w

7. Yang, X.;, Ullah, Z.; Stoddart, F.; Yavuz, C. Porous Organic Cages. Chem. Rev. 2023, 123, 4602–4634. DOI: 10.1021/acs.chemrev.2c00667

8. Xie, N.; Ma, D.-D.; Wu, X.-T.; Zhu, Q.-L. Facile construction of self-supported Fe-doped Ni3S2 nanoparticle arrays for the ultralow-overpotential oxygen evolution reaction. *Nanoscale* **2021,** *13* (3), 1807-1812, DOI: 10.1039/D0NR07262A

9. Wu, Z.-P.; Lu, X. F.; Zang, S.-Q.; Lou, X. W. Non-Noble-Metal-Based Electrocatalysts toward the Oxygen Evolution Reaction. *Adv. Funct. Mater.* **2020,** *30* (15), 1910274, DOI: 10.1002/adfm.201910274

10. Tang, S.; Zhang, Z.; Xiang, J.; Yang, X.; Shen, X.; Song, F. Recent advances in transition metal nitrides for hydrogen electrocatalysis in alkaline media: From catalyst design to application. *Front. Chem.* **2022,** *10*, 1073175, DOI: 10.3389/fchem.2022.1073175

11. Yoon, S.; Seo, H.; Jin, K.; Kim, H. G.; Lee, S.-Y.; Jo, J.; Cho, K. H.; Ryu, J.; Yoon, A.; Kim, Y.-W.; Zuo, J.-M.; Kwon, Y.-K.; Nam, K. T.; Kim, M. Atomic Reconstruction and Oxygen Evolution Reaction of Mn3O4 Nanoparticles. *J. Phys. Chem. Lett.* **2022,** *13* (35), 8336-8343, DOI: 10.1021/acs.jpclett.2c01638

12. Hu, M.; Ye, K.; Zhang, G.; Li, X.; Jiang, J. Insight into the Mechanism for Catalytic Activity of the Oxygen/Hydrogen Evolution Reaction on a Dual-Site Catalyst. *J. Phys. Chem. Lett.* **2023,** *14* (8), 2201-2207, DOI: 10.1021/acs.jpclett.3c00168

13. Oversteeg, C. H. M.; Doan, H. Q.; de Groot, F. M. F.; Cuk, T. In situ X-ray absorption spectroscopy of transition metal based water oxidation catalysts. *Chem. Soc. Rev.* **2017,** *46* (1), 102-125, DOI: 10.1039/C6CS00230G

14. Yagi, S.; Yamada, I.; Tsukasaki, H.; Seno, A.; Murakami, M.; Fujii, H.; Chen, H.; Umezawa, N.; Abe, H.; Nishiyama, N.; Mori, S. Covalency-reinforced oxygen evolution reaction catalyst. *Nat. Commun.* **2015,** *6* (1), 8249, DOI: 10.1038/ncomms9249

15. Viogradov, I.; Singh, S.; Lyle, H.; Paolino, M.; Mandal, A.; Rossmeisl, J.; Cuk, Tanja. Free energy difference to create the M-OH* intermediate of the oxygen evolution reaction by time-resolved optical spectroscopy. *Nat. Mater.* **2022**, *21*, 88-94. DOI: 10.1038/s41563-021-01118-9

16. Lv, L.; Yang, Z.; Chen, K.; Wang, C.; Xiong, Y. 2D Layered Double Hydroxides for Oxygen Evolution Reaction: From Fundamental Design to Application. *Adv. Energy Mater.* **2019,** *9* (17), 1803358, DOI: 10.1002/aenm.201803358

17. Gong, M.; Li, Y.; Wang, H.; Liang, Y.; Wu, J. Z.; Zhou, J.; Wang, J.; Regier, T.; Wei, F.; Dai, H. An Advanced Ni–Fe Layered Double Hydroxide Electrocatalyst for Water Oxidation. *J. Am. Chem. Soc.* **2013,** *135* (23), 8452-8455, DOI: 10.1021/ja4027715

18. Cai, Z.; Bu, X.; Wang, P.; Ho, J. C.; Yang, J.; Wang, X. Recent advances in layered double hydroxide electrocatalysts for the oxygen evolution reaction. *J. Mater. Chem. A* **2019,** *7* (10), 5069-5089, DOI: 10.1039/C8TA11273H

19. Chen, R.; Hung, S.-F.; Zhou, D.; Gao, J.; Yang, C.; Tao, H.; Yang, H. B.; Zhang, L.; Zhang, L.; Xiong, Q.; Chen, H. M.; Liu, B. Layered Structure Causes Bulk NiFe Layered Double Hydroxide Unstable in Alkaline Oxygen Evolution Reaction. *Adv. Mater.* **2019,** *31* (41), 1903909, DOI: 10.1002/adma.201903909

20. Trotochaud, L.; Young, S. L.; Ranney, J. K.; Boettcher, S. W. Nickel–Iron Oxyhydroxide Oxygen-Evolution Electrocatalysts: The Role of Intentional and Incidental Iron Incorporation. *J. Am. Chem. Soc.* **2014,** *136* (18), 6744-6753, DOI: 10.1021/ja502379c

21. Friebel, D.; Louie, M. W.; Bajdich, M.; Sanwald, K. E.; Cai, Y.; Wise, A. M.; Cheng, M.-J.; Sokaras, D.; Weng, T.-C.; Alonso-Mori, R.; Davis, R. C.; Bargar, J. R.; Nørskov, J. K.; Nilsson, A.; Bell, A. T. Identification of Highly Active Fe Sites in (Ni,Fe)OOH for Electrocatalytic Water Splitting. *J. Am. Chem. Soc.* **2015,** *137* (3), 1305-1313, DOI: 10.1021/ja511559d

22. Zhang, W.; Zhou, K. Ultrathin Two-Dimensional Nanostructured Materials for Highly Efficient Water Oxidation. *Small* **2017,** *13* (32), 1700806, DOI: 10.1002/smll.201700806

23. McCrory, C. C. L.; Jung, S.; Ferrer, I. M.; Chatman, S. M.; Peters, J. C.; Jaramillo, T. F., Benchmarking Hydrogen Evolving Reaction and Oxygen Evolving Reaction Electrocatalysts for Solar Water Splitting Devices. *J. Am. Chem. Soc.* **2015,** *137* (13), 4347-4357, DOI: 10.1021/ja510442p

24. Trotochaud, L.; Ranney, J. K.; Williams, K. N.; Boettcher, S. W., Solution-Cast Metal Oxide Thin Film Electrocatalysts for Oxygen Evolution. *J. Am. Chem. Soc.* **2012,** *134* (41), 17253-17261, DOI: 10.1021/ja307507a

25. Zhang, M.; Liu, Y.; Liu, B.; Chen, Z.; Xu, H.; Yan, K. Trimetallic NiCoFe-Layered Double Hydroxides Nanosheets Efficient for Oxygen Evolution and Highly Selective Oxidation of Biomass-Derived 5-Hydroxymethylfurfural. *ACS Catal.* **2020,** *10* (9), 5179-5189, DOI: 10.1021/acscatal.0c00007

26. Yang, X.; Chen, L.; Liu, H.; Kurihara, T.; HORIKE, S.; Xu, Q. Encapsulating Ultrastable Metal Nanoparticles

within Reticular Schiff Base Nanospaces for Enhanced Catalytic Performance. *Cell Rep. Phys. Sci.* **2021**, *2*, 100289, DOI: 10.1016/j.xcrp.2020.100289

27. Qu, G.; Zhou, Y.; Wu, T.; Zhao, G.; Li, F.; Kang, Y.; Xu, C. Phosphorized MXene-Phase Molybdenum Carbide as an Earth-Abundant Hydrogen Evolution Electrocatalyst. *ACS Appl. Energy Mater.* **2018,** *1* (12), 7206-7212, DOI: 10.1021/acsaem.8b01642
28. Mohammed-Ibrahim, J.; Sun, X. Recent progress on earth abundant electrocatalysts for hydrogen evolution reaction (HER) in alkaline medium to achieve efficient water splitting – A review. *J. Energy Chem.* **2019,** *34*, 111-160, DOI: 10.1016/j.jpowsour.2018.07.125
29. Yu, P.; Wang, F.; Shifa, T. A.; Zhan, X.; Lou, X.; Xia, F.; He, J. Earth abundant materials beyond transition metal dichalcogenides: A focus on electrocatalyzing hydrogen evolution reaction. *Nano Energy* **2019,** *58*, 244-276, DOI: 10.1016/j.nanoen.2019.01.017
30. Xie, J.; Yang, X.; Xie, Y. Defect engineering in two-dimensional electrocatalysts for hydrogen evolution. *Nanoscale* **2020,** *12* (7), 4283-4294, DOI: 10.1039/C9NR09753H
31. Naguib, M.; Kurtoglu, M.; Presser, V.; Lu, J.; Niu, J.; Heon, M.; Hultman, L.; Gogotsi, Y.; Barsoum, M. W. Two-Dimensional Nanocrystals Produced by Exfoliation of Ti3AlC2. *Adv. Mater.* **2011,** *23* (37), 4248-4253, DOI: 10.1002/adma.201102306
32. Anasori, B.; Lukatskaya, M. R.; Gogotsi, Y., 2D metal carbides and nitrides (MXenes) for energy storage. *Nat. Rev. Mater.* **2017,** *2* (2), 16098, DOI: 10.1038/natrevmats.2016.98
33. Shahzad, F.; Alhabeb, M.; Hatter, C. B.; Anasori, B.; Man Hong, S.; Koo, C. M.; Gogotsi, Y., Electromagnetic interference shielding with 2D transition metal carbides (MXenes). *Science* **2016,** *353* (6304), 1137-1140, DOI: 10.1126/science.aag2421
34. Ghidiu, M.; Lukatskaya, M. R.; Zhao, M.-Q.; Gogotsi, Y.; Barsoum, M. W. Conductive two-dimensional titanium carbide 'clay' with high volumetric capacitance. *Nature* **2014,** *516* (7529), 78-81 DOI: 10.1038/nature13970
35. Naguib, M.; Mashtalir, O.; Carle, J.; Presser, V.; Lu, J.; Hultman, L.; Gogotsi, Y.; Barsoum, M. W. Two-Dimensional Transition Metal Carbides. *ACS Nano* **2012,** *6* (2), 1322-1331, DOI: 10.1021/nn204153h
36. Lukatskaya, M. R.; Kota, S.; Lin, Z.; Zhao, M.-Q.; Shpigel, N.; Levi, M. D.; Halim, J.; Taberna, P.-L.; Barsoum, M. W.; Simon, P.; Gogotsi, Y. Ultra-high-rate pseudocapacitive energy storage in two-dimensional transition metal carbides. *Nat. Energy* **2017,** *2* (8), 17105, DOI: 10.1038/nenergy.2017.105
37. Zhang, Y.-Z.; El-Demellawi, J. K.; Jiang, Q.; Ge, G.; Liang, H.; Lee, K.; Dong, X.; Alshareef, H. N. MXene hydrogels: fundamentals and applications. *Chem. Soc. Rev.* **2020,** *49* (20), 7229-7251, DOI: 10.1039/D0CS00022A
38. Shin, H.; Eom, W.; Lee, K. H.; Jeong, W.; Kang, D. J.; Han, T. H. Highly Electroconductive and Mechanically Strong Ti3C2Tx MXene Fibers Using a Deformable MXene Gel. *ACS Nano* **2021,** *15* (2), 3320-3329, DOI: 10.1021/acsnano.0c10255
39. Pan, X.; Jiang, S.; Zhang, Q.; Luo, Y. Tracking the Explosive Boiling Dynamics at the Alcohol/MXene Interface. *J. Phys. Chem. Lett.* **2023,** *14* (18), 4142-4149, DOI: 10.1021/acs.jpclett.3c00472
40. Zhang, J.; Zhao, Y.; Guo, X.; Chen, C.; Dong, C.-L.; Liu, R.-S.; Han, C.-P.; Li, Y.; Gogotsi, Y.; Wang, G. Single platinum atoms immobilized on an MXene as an efficient catalyst for the hydrogen evolution reaction. *Nat. Catal.* **2018,** *1* (12), 985-992, DOI: 10.1038/s41929-018-0195-1
41. Lim, K. R. G.; Handoko, A. D.; Johnson, L. R.; Meng, X.; Lin, M.; Subramanian, G. S.; Anasori, B.; Gogotsi, Y.; Vojvodic, A.; Seh, Z. W. 2H-MoS2 on Mo2CTx MXene Nanohybrid for Efficient and Durable Electrocatalytic Hydrogen Evolution. *ACS Nano* **2020,** *14* (11), 16140-16155, DOI: 10.1021/acsnano.0c08671
42. Satheeshkumar, E.; Makaryan, T.; Melikyan, A.; Minassian, H.; Gogotsi, Y.; Yoshimura, M. One-step Solution Processing of Ag, Au and Pd@MXene Hybrids for SERS. *Sci. Rep.* **2016,** *6* (1), 32049, DOI: 10.1038/srep32049
43. Yue, Q.; Sun, J.; Chen, S.; Zhou, Y.; Li, H.; Chen, Y.; Zhang, R.; Wei, G.; Kang, Y. Hierarchical Mesoporous MXene–NiCoP Electrocatalyst for Water-Splitting. *ACS Appl. Mater. Interfaces* **2020,** *12* (16), 18570-18577, DOI: 10.1021/acsami.0c01303
44. Fu, S.; Song, J.; Zhu, C.; Xu, G.-L.; Amine, K.; Sun, C.; Li, X.; Engelhard, M. H.; Du, D.; Lin, Y. Ultrafine and highly disordered Ni2Fe1 nanofoams enabled highly efficient oxygen evolution reaction in alkaline electrolyte. *Nano Energy* **2018,** *44*, 319-326, DOI: 10.1016/j.nanoen.2017.12.010
45. Zhou, Q.; Chen, Y.; Zhao, G.; Lin, Y.; Yu, Z.; Xu, X.; Wang, X.; Liu, H. K.; Sun, W.; Dou, S. X. Active-Site-Enriched Iron-Doped Nickel/Cobalt Hydroxide Nanosheets for Enhanced Oxygen Evolution Reaction. *ACS Catal.* **2018,** *8* (6), 5382-5390, DOI: 10.1021/acscatal.8b01332
46. Chen, J. Y. C.; Dang, L.; Liang, H.; Bi, W.; Gerken, J. B.; Jin, S.; Alp, E. E.; Stahl, S. S. Operando Analysis of NiFe and Fe Oxyhydroxide Electrocatalysts for Water Oxidation: Detection of Fe4+ by Mössbauer Spectroscopy. *J. Am. Chem. Soc.* **2015,** *137* (48), 15090-15093, DOI: 10.1021/jacs.5b10699
47. Zhang, T.; Song, F.; Qian, Y.; Gao, H.; Shaw, J.; Rao, Y. Elemental Engineering of High-Charge-Density Boron

in Nickel as Multifunctional Electrocatalysts for Hydrogen Oxidation and Water Splitting. *ACS Appl. Energy Mater.* **2021,** *4* (6), 5434-5442, DOI: 10.1021/acsaem.0c03179

48. Song, F.; Zhang, T.; Zhou, D.; Sun, P.; Lu, Z.; Bian, H.; Dang, J.; Gao, H.; Qian, Y.; Li, W.; Jiang, N.; Dummer, H.; Shaw, J. G.; Chen, S.; Chen, G.; Sun, Y.; Rao, Y. Charge Transfer of Interfacial Catalysts for Hydrogen Energy. *ACS Mater. Lett.* **2022,** *4* (5), 967-977, DOI: 10.1021/acsmaterialslett.2c00143
49. Li, J.; Zou, S.; Liu, X.; Lu, Y.; Dong, D., Electronically Modulated CoP by Ce Doping as a Highly Efficient Electrocatalyst for Water Splitting., *ACS Sustainable Chem. Eng.* **2020,** *8* (27), 10009-10016, DOI: 10.1021/acssuschemeng.0c01193
50. Chauhan, M.; Deka, S. Hollow Cobalt Sulfide Nanoparticles: A Robust and Low-Cost pH-Universal Oxygen Evolution Electrocatalyst. *ACS Appl. Energy Mater.* **2020,** *3* (1), 977-986, DOI: 10.1021/acsaem.9b02019
51. Han, X.; Zhang, W.; Ma, X.; Zhong, C.; Zhao, N.; Hu, W.; Deng, Y., Identifying the Activation of Bimetallic Sites in NiCo2S4@g-C3N4-CNT Hybrid Electrocatalysts for Synergistic Oxygen Reduction and Evolution. *Adv. Mater.* **2019,** *31* (18), 1808281, DOI: 10.1002/adma.201808281
52. Xue, S.; Chen, L.; Liu, Z.; Cheng, H.-M.; Ren, W. NiPS3 Nanosheet–Graphene Composites as Highly Efficient Electrocatalysts for Oxygen Evolution Reaction. *ACS Nano* **2018,** *12* (6), 5297-5305, DOI: 10.1021/acsnano.7b09146
53. Yu, C.; Liu, Z.; Han, X.; Huang, H.; Zhao, C.; Yang, J.; Qiu, J. NiCo-layered double hydroxides vertically assembled on carbon fiber papers as binder-free high-active electrocatalysts for water oxidation. *Carbon* **2016,** *110*, 1-7, DOI: 10.1016/j.carbon.2016.08.020
54. Burke, M. S.; Kast, M. G.; Trotochaud, L.; Smith, A. M.; Boettcher, S. W. Cobalt–Iron (Oxy)hydroxide Oxygen Evolution Electrocatalysts: The Role of Structure and Composition on Activity, Stability, and Mechanism. *J. Am. Chem. Soc.* **2015,** *137* (10), 3638-3648, DOI: 10.1021/jacs.5b00281
55. Masa, J.; Weide, P.; Peeters, D.; Sinev, I.; Xia, W.; Sun, Z.; Somsen, C.; Muhler, M.; Schuhmann, W. Amorphous Cobalt Boride (Co2B) as a Highly Efficient Nonprecious Catalyst for Electrochemical Water Splitting: Oxygen and Hydrogen Evolution. *Adv. Energy Mater.* **2016,** *6* (6), 1502313, DOI: 10.1002/aenm.201502313
56. Wu, D.; Wei, Y.; Ren, X.; Ji, X.; Liu, Y.; Guo, X.; Liu, Z.; Asiri, A. M.; Wei, Q.; Sun, X., Co(OH)2 Nanoparticle-Encapsulating Conductive Nanowires Array: Room-Temperature Electrochemical Preparation for High-Performance Water Oxidation Electrocatalysis. *Adv. Mater.* **2018,** *30* (9), 1705366, DOI: 10.1002/adma.201705366
57. Xie, L.; Tang, C.; Wang, K.; Du, G.; Asiri, A. M.; Sun, X. Cu(OH)2@CoCO3(OH)2·nH2O Core–Shell Heterostructure Nanowire Array: An Efficient 3D Anodic Catalyst for Oxygen Evolution and Methanol Electrooxidation. *Small* **2017,** *13* (7), 1602755, DOI: 10.1002/smll.201602755
58. Huang, J.; Xu, P.; Gao, T.; Huangfu, J.; Wang, X.-j.; Liu, S.; Zhang, Y.; Song, B. Controlled Synthesis of Hollow Bimetallic Prussian Blue Analog for Conversion into Efficient Oxygen Evolution Electrocatalyst. *ACS Sustainable Chem. Eng.* **2020,** *8* (2), 1319-1328, DOI: 10.1021/acssuschemeng.9b07122
59. Liu, T.; Asiri, A. M.; Sun, X., Electrodeposited Co-doped NiSe2 nanoparticles film: a good electrocatalyst for efficient water splitting. *Nanoscale* **2016,** *8* (7), 3911-3915, DOI: 10.1039/C5NR07170D
60. Qi, Y.; Wu, J.; Xu, J.; Gao, H.; Du, Z.; Liu, B.; Liu, L.; Xiong, D., One-step fabrication of a self-supported Co@CoTe2 electrocatalyst for efficient and durable oxygen evolution reactions. *Inorg. Chem. Front.* **2020,** *7* (13), 2523-2532, DOI: 10.1039/D0QI00372G
61. Kou, Z.; Wang, K.; Liu, Z.; Zeng, L.; Li, Z.; Yang, B.; Lei, L.; Yuan, C.; Hou, Y., Recent Advances in Manifold Exfoliated Synthesis of Two-Dimensional Non-precious Metal-Based Nanosheet Electrocatalysts for Water Splitting. *Small Struct.* **2022,** *3* (1), 2100153, DOI: 10.1002/sstr.202100153
62. Anjum, M. A. R.; Bhatt, M. D.; Lee, M. H.; Lee, J. S., Sulfur-Doped Dicobalt Phosphide Outperforming Precious Metals as a Bifunctional Electrocatalyst for Alkaline Water Electrolysis. *Chem. Mater.* **2018,** *30* (24), 8861-8870, DOI: 10.1021/acs.chemmater.8b03908
63. Song, F.; Zhang, T.; Qian, Y.; Shaw, J.; Chen, S.; Chen, G.; Sun, Y.; Rao, Y., Multifunctional electrocatalysts of nickel boride nanoparticles for superior hydrogen oxidation and water splitting. *Mater. Today Energy* **2021,** *22*, 100846, DOI: 10.1016/j.mtener.2021.100846
64. Yang, L.; Xu, H.; Liu, H.; Cheng, D.; Cao, D., Active Site Identification and Evaluation Criteria of In Situ Grown CoTe and NiTe Nanoarrays for Hydrogen Evolution and Oxygen Evolution Reactions. *Small Methods* **2019,** *3* (5), 1900113, DOI: 10.1002/smtd.201900113
65. Das, D.; Nanda, K. K., One-step, integrated fabrication of Co2P nanoparticles encapsulated N, P dual-doped CNTs for highly advanced total water splitting. *Nano Energy* **2016,** *30*, 303-311, DOI: 10.1016/j.nanoen.2016.10.024
66. Zeng, X.; Ye, Y.; Wang, Y.; Yu, R.; Moskovits, M.; Stucky, G. D., Honeycomb-like MXene/NiFePx–NC with "continuous" single-crystal enabling high activity and robust durability in electrocatalytic oxygen evolution reactions. *J. Adv. Ceram.* **2023,** *12* (3), 553-564, DOI: 10.26599/JAC.2023.9220704
67. Li, K.; Pan, S.; Zhang, H.; Zhang, Q.; Wa, D.; Zeng, X., Interfacial engineering and chemical reconstruction of

Mo/Mo2C@CoO@NC heterostructure for promoting oxygen evolution reaction. *Dalton T.* **2023,** *52* (9), 2693-2702, DOI: 10.1039/D2DT03865J
68. Zeng, X.; Tan, Y.; Xia, L.; Zhang, Q.; Stucky, G. D., MXene-derived Ti3C2–Co–TiO2 nanoparticle arrays via cation exchange for highly efficient and stable electrocatalytic oxygen evolution. *Chem. Commun.* **2023,** *59* (7), 880-883, DOI: 10.1039/D2CC05911H
69. Nørskov, J. K.; Rossmeisl, J.; Logadottir, A.; Lindqvist, L.; Kitchin, J. R.; Bligaard, T.; Jónsson, H., Origin of the Overpotential for Oxygen Reduction at a Fuel-Cell Cathode. *J. Phys. Chem. B* **2004,** *108* (46), 17886-17892, DOI: 10.1021/jp047349j
70. Man, I. C.; Su, H.-Y.; Calle-Vallejo, F.; Hansen, H. A.; Martínez, J. I.; Inoglu, N. G.; Kitchin, J.; Jaramillo, T. F.; Nørskov, J. K.; Rossmeisl, J., Universality in Oxygen Evolution Electrocatalysis on Oxide Surfaces. *ChemCatChem* **2011,** *3* (7), 1159-1165, DOI: 10.1002/cctc.201000397
71. Yu, L.; Hu, L.; Anasori, B.; Liu, Y.-T.; Zhu, Q.; Zhang, P.; Gogotsi, Y.; Xu, B., MXene-Bonded Activated Carbon as a Flexible Electrode for High-Performance Supercapacitors. *ACS Energy Lett.* **2018,** *3* (7), 1597-1603, DOI: 10.1021/acsenergylett.8b00718
72. Moschkowitsch, W.; Dhaka, K.; Gonen, S.; Attias, R.; Tsur, Y.; Caspary Toroker, M.; Elbaz, L., Ternary NiFeTiOOH Catalyst for the Oxygen Evolution Reaction: Study of the Effect of the Addition of Ti at Different Loadings. *ACS Catal.* **2020,** *10* (9), 4879-4887, DOI: 10.1021/acscatal.0c00105

TOC Graphic

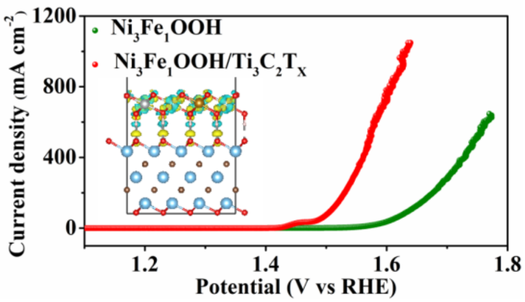
Current density (mA cm^{-2})
1200
800
400
0
1.2
1.4
1.6
1.8
Potential (V vs RHE)
● Ni_3Fe_1OOH
● $Ni_3Fe_1OOH/Ti_3C_2T_X$